JOURNAL OF SPACECRAFT AND ROCKETS
Vol. 57, No. 6, November–December 2020

Validating the Deployment of a Novel Tether Design for Orbital Debris Removal

Kevin Stadnyk* and Steve Ulrich†
Carleton University, Ottawa, Ontario K1S 5B6, Canada

https://doi.org/10.2514/1.A34781

With the global push to commercialize space, humans are launching objects into orbit faster than natural effects are removing them. Orbital debris is especially dangerous because it is capable of exponential growth due to cascading collisions between orbiting objects. To ensure the long-term accessibility to space, high-risk objects must be actively removed to limit growth of the orbital debris population. One method of active debris removal is with a tethered net to capture and tow an object out of orbit. This work presents the validation of a proposed novel tether configurations deployment dynamics. Tether elements are simulated using two numerical models: a lumped mass node system connected by massless spring–damper elements, and an absolute nodal coordinate formulation model. Their accuracy to predict the deployment motion of a tether is experimentally determined, and a complete capture scenario using the novel tether design is presented for the first time.

Nomenclature

A	=	cross-sectional area, m^2
$\mathbf{C}_{AB}$	=	rotation matrix from A to B
c	=	damping coefficient, $(N \cdot s)/m$
$\mathbf{d}$	=	deployment direction vector components of a tether bullet
E	=	elastic Young's modulus, Pa
$\boldsymbol{e}_x$	=	absolute nodal coordinates of a tether element at length x
F	=	force magnitude, N
$\mathbf{F}$	=	force vector components, N
$\mathcal{F}_x$	=	vectrix of reference frame x
I	=	area moment of inertia of a tether cross section, m^4
$\mathbf{I}_{x\times y}$	=	identity matrix of dimension x by y
J	=	moment of inertia, kg/m^2
k	=	stiffness, N/m
$\mathbf{L}$	=	tether element stretch as vector components, m
L_0	=	length of an unstretched tether element, m
m	=	mass, kg
$\mathbf{q}$	=	quaternion
$\mathbf{r}$	=	position vector components, m
$\mathbf{S}$	=	shape function
S_x	=	shape function component x
U_b	=	strain energy due to bending, $kg/m^2/s^2$
U_l	=	strain energy due to longitudinal deformation, $kg/m^2/s^2$
β	=	Newmark-beta integration coefficient
γ	=	Newmark-beta integration coefficient
ΔL	=	tether element stretch magnitude, m
ε_l	=	axial strain
ζ	=	damping ratio
θ	=	angle, deg
κ	=	curvature, m^{-1}
μ	=	gravitational parameter of the Earth, m^3/s^2
ρ	=	density, kg/m^3
τ	=	torque, N/m
ϕ	=	tether angle, deg
χ_x	=	tether attachment point on body x with respect to its center of mass, m
ψ	=	fractional length along a tether element, m
ω	=	angular rate, deg/s

Presented as Paper 2020-0719 at the AIAA SciTech 2020 Forum, Orlando, Florida, January 6–10, 2020; received 13 February 2020; revision received 14 May 2020; accepted for publication 20 May 2020; published online 17 July 2020.

*Graduate Student, Department of Mechanical and Aerospace Engineering, 1125 Colonel By Drive.

†Associate Professor, Department of Mechanical and Aerospace Engineering, 1125 Colonel By Drive. Senior Member AIAA.

I. Introduction

THE term *orbital debris* refers to objects in orbit around Earth that are not considered useful. Due to the vastness of space, orbital debris was thought to pose no risk to future spacefaring missions until proven otherwise by by Donald J. Kessler and Burton G. Cour-Palais [1]. Known as the *Kessler syndrome*, Kessler and Cour-Palais stated that eventual collisions between orbital objects will lead to sequential collisions, producing new debris, and ultimately create a chain reaction that will grow the debris population faster than it can naturally decay. According to a NASA model [2], 5–10 high-risk debris objects must be actively removed from orbit each year to stabilize the low-Earth-orbit (LEO) environment.

Of the many phases of an active space debris removal mission, the deployment, contact, and stabilization phases are among the most important. When using a tethered-net method of capture, there is only one chance to capture the target debris, which becomes a more complicated task when the debris is tumbling. That is, it has angular rates about all three axes. If the debris were to be spinning slowly even about three axes, the chaser spacecraft could match the angular rates of the debris and remove any relative motion between the two objects, greatly simplifying the problem. When this is not the case, a different approach must be taken.

Various methods of orbital debris removal have been proposed [3–5]. Flexible connection methods [6–8], in which the chaser spacecraft and debris are connected by a flexible tether, are of interest because they encompass both net and harpoon capture methods. Of these, tethered-net capture methods are particularly interesting because they can capture debris of any size, they do not require a specific grappling point, they can capture debris tumbling with high angular rates, and they interface well with the proposed novel tether design.

Net capturing consists of a net with weighted corners, henceforth referred to as bullets, which are launched at an outward angle in the direction of the debris. The bullets pull on the folded net, causing it to expand in flight before reaching the debris. On contact, the net will completely envelop the debris. The corner weights can become tangled within themselves to secure the debris, or a net closing mechanism may be used [9]. Tethered-net capture has been shown both numerically [8,10–13] and experimentally [10,12,14–17], with parabolic flights being used to conduct experiments in a microgravity environment. Net capture has been demonstrated in an orbital environment during the RemoveDEBRIS demonstrator mission [18]; however, the tether was released from the spacecraft because full tethered-net capture was beyond the scope of the mission.

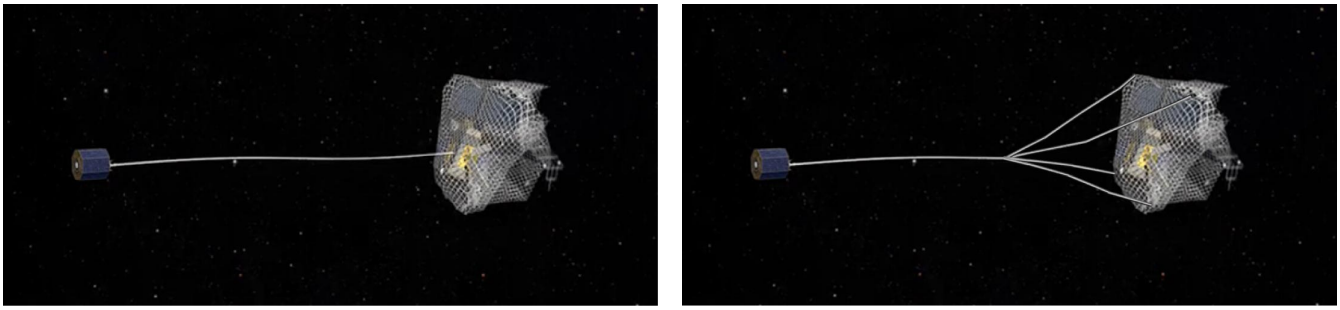

a) Single tether configuration

b) Subtether configuration [20–23]

Fig. 1 Single and subtether tethered-net configurations.

Although research has been previously conducted on the dynamics of spacecraft connected by flexible tethers [19], it has always used a single tether between the chaser and debris. Hovell and Ulrich [20–23] were the first to propose a novel tether design to improve upon traditional single tether configurations. The novel tether comprises a single tether stemming from the chaser to a midpoint denoted as the junction. From this point, the tether branches out into four individual tethers, denoted as subtethers, with each attached to the net at their ends. Depictions of a traditional tether configuration alongside the novel tether configuration are seen in Fig. 1.

The reason the novel tether configuration interfaces with a net is because all subtethers are required to attach to the target in order to maximize its stabilization effects while in tension. If harpoons were attached to the ends of the subtethers instead of a net, it would greatly increase the complexity of a space debris removal mission by requiring all harpoons to contact the target: ideally, at equally spaced locations. This is an already difficult feat, which becomes even more difficult when the target is tumbling. For this reason, a net has been chosen as the best method of establishing a connection between a target debris object and a debris removal spacecraft when using the novel tether design.

It has been demonstrated both experimentally and in simulations that, although the novel tether configuration is in tension, it is capable of passively reducing the angular rates of the captured debris using its viscoelastic properties. Their findings lead to the proposal of two debris detumbling methods using the novel tether configuration. The first method involves the chaser spacecraft accelerating away from the captured debris to maintain tension in the tether. The second method involves the chaser spacecraft initiating a spin on the tethered-spacecraft system to maintain tension on the tether.

To date, all detumbling simulations and experiments using the novel tether configuration were performed with both the chaser spacecraft and debris initially tethered together. This work is concerned first with the deployment dynamics of the novel tether and second with creating a complete capture scenario using the novel tether configuration. It is important to note that, in order to focus on the deployment and postcapture dynamics of the novel tether configuration, a net is omitted at the end of subtethers. This is done in simulations in order to isolate the novel tether configuration, and in experiments due to constraints of the laboratory environment. This works contributions to the field include the validation of massless spring–damper and absolute nodal coordinate frame numerical models when used to model the novel tether configuration and, for the first time, the demonstration of a complete capture scenario using the novel tether configuration in both simulation and experiment.

This remainder of this paper is organized as follows: Sec. II outlines the numerical methods used to model the spacecraft, debris, and tethers during deployment and stabilization phases; Sec. III presents the results of an orbital complete capture scenario; Sec. IV presents the results of both the tether deployment and complete capture scenario experiments; and, lastly, Sec. V summarizes the work presented in this paper.

II. Spacecraft and Tether Dynamics

High-fidelity numerical simulations are useful for understanding how a tether is deployed from a spacecraft in an orbital environment. By modeling the dynamics of a chaser spacecraft and tether, including perturbations present in the orbital environment, an accurate tether deployment scenario can be investigated. This section presents the dynamical motion of a chaser spacecraft and debris, two tether models, and the postcapture tethered-spacecraft-system (TSS) dynamics. It builds on work from Hovell and Ulrich [23] to bring together the deployment and postcapture stabilization phases in order to demonstrate a complete capture scenario using the novel tether. Similarly to Shan [9], who studied space-based net dynamics, the tether deployment dynamics in this work are modeled with two different numerical models. The first model presented comprises lumped mass nodes connected by massless spring–damper elements. The second model approximates the tethers using absolute nodal coordinate formulation (ANCF) beam elements that are so thin they act as flexible tethers. Both models ignore torsion, and the spring–damper model ignores bending effects. A net modeled at the end of the tethers is omitted because it is not compatible in the laboratory environment used to validate the numerical models.

A. Model Reference Frame

In modeling the orbital environment of the spacecraft and tethers, $\mathcal{F}_I$ represents an inertially fixed reference frame, and the position of the debris is described by the vector $\boldsymbol{r}_t$. These are used to calculate $\mathbf{r}_t$, representing the three-dimensional components of the debris center of mass position vector in the inertially fixed reference frame

$$\boldsymbol{r}_t = \boldsymbol{\mathcal{F}}_I^{\mathrm{T}} \mathbf{r}_t \tag{1}$$

The chaser and all tether nodes are represented as point masses. Their locations are, respectively, described by position vectors $\boldsymbol{r}_c$ and $\boldsymbol{r}_{n_i}$ such that

$$\boldsymbol{r}_c = \boldsymbol{\mathcal{F}}_I^{\mathrm{T}} \mathbf{r}_c \tag{2}$$

$$\boldsymbol{r}_{n_i} = \boldsymbol{\mathcal{F}}_I^{\mathrm{T}} \mathbf{r}_{n_i} \tag{3}$$

where $\mathbf{r}_c$ and $\mathbf{r}_{n_i}$ are the three-dimensional components of the chaser and ith node position vectors in the inertially fixed reference frame, respectively.

B. Attitude Motion

Euler's equations of motion are used to describe the debris angular rates in the body-fixed reference frame $\mathcal{F}_B$ [24]. This is given by

$$\mathbf{J}\boldsymbol{\omega} + \boldsymbol{\omega}^{\times}(\mathbf{J}\boldsymbol{\omega}) = \boldsymbol{\tau} \tag{4}$$

where $\boldsymbol{\omega}$ are the components of the angular rate vector in $\mathcal{F}_B$, $\mathbf{J}$ is the inertia matrix of the debris, and $\boldsymbol{\tau}$ is the sum of external torque applied to the debris.

By assuming that $\mathcal{F}_B$ is aligned with the principal axes of the body, $\mathbf{J}$ can be simplified to

$$\mathbf{J} = \begin{bmatrix} J_{xx} & 0 & 0 \\ 0 & J_{yy} & 0 \\ 0 & 0 & J_{zz} \end{bmatrix} \tag{5}$$

where J_{xx}, J_{yy}, and J_{zz} are the principal moments of inertia of the debris.

The attitude of the debris is described using quaternion kinematics [24]

$$\dot{\mathbf{q}} = \frac{1}{2}\begin{bmatrix} (\boldsymbol{\epsilon}^{\times} + \eta \mathbf{I}_{3\times 3})\boldsymbol{\omega} \\ -\boldsymbol{\epsilon}^{\mathrm{T}}\boldsymbol{\omega} \end{bmatrix} \tag{6}$$

where $\mathbf{q}$ represents the attitude quaternion in $\mathcal{F}_B$ with respect to the inertially fixed reference frame $\mathcal{F}_I$. It is defined as

$$\mathbf{q} = \begin{bmatrix} q_1 \\ q_2 \\ q_3 \\ q_4 \end{bmatrix} = \begin{bmatrix} \boldsymbol{\epsilon} \\ \eta \end{bmatrix} = \begin{bmatrix} \boldsymbol{b}\cos\left(\frac{\phi}{2}\right) \\ \sin\left(\frac{\phi}{2}\right) \end{bmatrix} \tag{7}$$

where $\boldsymbol{b}$ is the axis of rotation, ϕ is the angle of rotation, and

$$\boldsymbol{\epsilon} = \begin{bmatrix} q_1 \\ q_2 \\ q_3 \end{bmatrix} \tag{8}$$

$$\eta = q_4 \tag{9}$$

An additional perturbation affecting the debris attitude is the gravity-gradient torque, which is due to the inverse square law of the gravitational field of the Earth. This causes an unequal gravitational force acting across the debris body, leading to restoring torques acting on it [24]. These restoring torque effects are significant in LEO. The effect is quantified through

$$\boldsymbol{\tau}_g = \frac{3\mu}{\|\mathbf{r}_t^b\|^5}\mathbf{r}_t^{b\times}\mathbf{J}\mathbf{r}_t^b \tag{10}$$

where $\boldsymbol{\tau}_g$ are the resulting gravity-gradient torque components in $\mathcal{F}_B$, μ is the gravitational parameter of Earth, and $\mathbf{r}_t^b$ are the components of the debris position vector expressed in $\mathcal{F}_B$ as

$$\mathbf{r}_t^b = \mathbf{C}_{\mathrm{BI}}(\mathbf{q})\mathbf{r}_t \tag{11}$$

where the rotation matrix $\boldsymbol{C}_{\mathrm{BI}}(\boldsymbol{q})$ represents a rotation from $\mathcal{F}_I$ to $\mathcal{F}_B$. This is obtained from the quaternion $\mathbf{q}$ by

$$\mathbf{C}_{\mathrm{BI}}(\mathbf{q}) = \begin{bmatrix} 1-2q_2^2-2q_3^2 & 2(q_1q_2+q_4q_3) & 2(q_1q_3-q_4q_2) \\ 2(q_1q_2-q_4q_3) & 1-2q_1^2-2q_3^2 & 2(q_2q_3+q_4q_1) \\ 2(q_1q_3+q_4q_2) & 2(q_2q_3-q_4q_1) & 1-2q_1^2-2q_2^2 \end{bmatrix} \tag{12}$$

C. Translational Motion

To model the debris, chaser spacecraft, and tether node linear motion, Newton's second law is used:

$$\mathbf{F} = m\ddot{\mathbf{r}} \tag{13}$$

where $\mathbf{F}$ are the components of the net force applied to the body, m is the mass of the body in question, and $\ddot{\mathbf{r}}$ is the inertial linear acceleration.

The force due to gravity acting on the orbiting spacecraft or tether node $\mathbf{F}_g$ is described by Newton's law of gravitation:

$$\mathbf{F}_g = -\frac{\mu m}{\|\mathbf{r}\|^3}\mathbf{r} \tag{14}$$

where $\mathbf{r}$ is the components of the position vector of the orbiting spacecraft or tether node in $\mathcal{F}_I$. Newton's law of gravitation applies to the chaser spacecraft, debris, and tether nodes.

During deployment, while the tether is not under tension, forces exerted on the chaser spacecraft are due to the impulse generated during tether deployment and its orbital motion. No forces due to the tether are exerted on the debris. Post contact, the main tether and subtethers generate external forces while in tension, which are applied to each spacecraft mass.

D. Lumped Mass Node and Massless Spring–Damper Model

During tether deployment, the spring–damper model approximates the tether as a series of lumped mass nodes connected by massless spring–damper elements. The tether is discretized into many nodes along its length. Force acting on the ith node generated by the jth node connected to it is as given as

$$F_{ij} = -k(r_{ij} - L_0) - c\dot{r}_{ij} \tag{15}$$

where k is the axial stiffness, c is the damping coefficient, L_0 is the unstretched length of a tether segment between the ith and jth nodes, and lastly r_{ij} and $\dot{r}_{ij}$ are the relative positions and velocities between the ith and jth tether nodes, respectively.

By assuming the tether material is a homogeneous isotropic linear material, the axial stiffness of the tether is defined as

$$k = \frac{EA}{L_0} \tag{16}$$

where E is the elastic Young's modulus of the tether material, and A is the cross-sectional area of the tether.

The damping coefficient is dependent on the tether material. It is a function of the node mass m_i stiffness and damping ratio ζ given as

$$c = 2\zeta\sqrt{m_i k} \tag{17}$$

In accordance with the tether material, a tension force is only generated when the element is elongated, and elements of the tether are not able to withstand compression. This gives the applied force conditions of

$$\mathbf{F}_{ij} = \begin{cases} F_{ij}\dfrac{\mathbf{r}_{ij}}{\|\mathbf{r}_{ij}\|}, & \text{for } r_{ij} > L_0 \\ 0, & \text{otherwise} \end{cases} \tag{18}$$

The lumped mass distribution of each node is modeled as the half-masses of the number of adjacent nodes and the cross-sectional area of each tether segment to any given node. The tether has three distinct node masses, with the mass of the ith node given as

$$m_i = \begin{cases} m_b, & \text{for } i \text{ at the tether end} \\ \rho A l_0, & \text{for } i \text{ along the tether} \\ \dfrac{3}{2}\rho A L_0, & \text{for } i \text{ at the tether junction} \end{cases} \tag{19}$$

where ρ is the material density of the tether.

E. Absolute Nodal Coordinate Formulation Model

The ANCF was first proposed by Shabana et al. [25] and stems from traditional finite element methods. It is most commonly found in applications related to beam bending and large displacement and deformation problems. In the ANCF model, a tether is approximated by a beam with a very small cross-sectional area relative to its length, allowing it to become very flexible. The absolute nodal coordinates $\boldsymbol{e}_i$ of a given node in the tether element comprise the global displacement and slope of the element, $\boldsymbol{r}_i$ and $\boldsymbol{r}_{ix}$, respectively. It is expressed as

$$\mathbf{e}_i = [\mathbf{r}_i, \mathbf{r}_{ix}] \tag{20}$$

where

$$\mathbf{r}_{ix} = \frac{\partial \mathbf{r}_i}{\partial x} \tag{21}$$

An arbitrary position in a cable element $\mathbf{r}_x$ is determined by the shape function $\mathbf{S}$ and the absolute nodal coordinates of the tether at the lengths of $x = 0$ and $x = L_0$. This is expressed as

$$\mathbf{r}_x = \mathbf{Se} = [\mathbf{S}_1\mathbf{I}_{3\times3}, \mathbf{S}_2\mathbf{I}_{3\times3}, \mathbf{S}_3\mathbf{I}_{3\times3}, \mathbf{S}_4\mathbf{I}_{3\times3}][\mathbf{e}_{x=0}, \mathbf{e}_{x=L_0}]^T \tag{22}$$

with the elements of the shape function taking the form

$$\begin{aligned} S_1 &= 1 - 3\psi^2 + 2\psi^3 \\ S_2 &= L_0(\psi - 2\psi^2 + \psi^3) \\ S_3 &= 3\psi^2 + 2\psi^3 \\ S_4 &= L_0(-\psi^2 + \psi^3) \end{aligned} \tag{23}$$

where $\mathbf{I}_{3\times3}$ is the 3×3 identity matrix, ψ is the fractional length along the tether where $\psi = (x/L_0)$, and x is the coordinate of an arbitrary point along the tether element. It is assumed that the y and z directions are not accounted for because the magnitude of the displacement in those directions is very small compared to the magnitude of the displacement in x.

When the tether is in tension, elastic forces are applied based on an elastic energy model. The elastic forces are made up of two parts: the strain energy due to longitudinal deformation U_l, and the strain energy due to bending U_b. They are expressed as

$$U_l = \frac{1}{2}\int_0^{L_0} EA\varepsilon_l^2 \, \mathrm{d}x \tag{24}$$

$$U_b = \frac{1}{2}\int_0^{L_0} EI\kappa^2 \, \mathrm{d}x \tag{25}$$

where the axial strain ε_l is expressed based on Cauchy–Green longitudinal strain, and the curvature κ is derived from the Serret–Frenet frame [26].

Using the strain energy, the elastic forces in a tether element are calculated as

$$\mathbf{F}_i = \left(\frac{\partial U}{\partial \boldsymbol{e}_i}\right)^T \tag{26}$$

The acceleration, velocity, and position of tether nodes are calculated using the Newmark-beta integration method [27]:

$$\dot{u}_{n+1} = \dot{u}_n + \Delta t\{(1-\gamma)\ddot{u}_n + \gamma\ddot{u}_{n+1}\} \tag{27}$$

and

$$u_{n+1} = u_n + \Delta t\dot{u}_n + \frac{1}{2}\Delta t^2(1-2\beta)\ddot{u}_n + 2\beta\ddot{u}_{n+1} \tag{28}$$

where γ and β are coefficients bounded by $0 \le \gamma \le 1$ and $0 \le 2\beta \le 1$, respectively; and Δt is the simulation time step.

F. Postcapture Spring–Damper Tether Model

Following Hovell and Ulrich's [23] work, during the postcapture phase, tethers are modeled as a single massless spring–damper element between the spacecraft body and junction. Torsion and bending effects are ignored. External forces are only generated while the tether elements are in tension, and they are applied to each connected mass.

Defining the ith subtether under analysis by the vector $\boldsymbol{L}_i$ in $\mathcal{F}_I$ has the component form of

$$\mathbf{L}_i = \mathbf{r}_{n_i} - \mathbf{r}_t - \mathbf{C}_{\mathrm{BI}}(\mathbf{q})^{\mathrm{T}}\chi_{t,i}, \quad \forall\ i = 1, \ldots, 4 \tag{29}$$

where $\chi_{t,i}$ is the attachment point of the ith subtether relative to the center of mass of the debris in $\mathcal{F}_B$.

By treating the linear spring and damper in parallel, the resultant tensile force magnitude developed by the ith subtether is

$$F_i = \begin{cases} k(\|\mathbf{L}_i\| - L_0) + c[\mathbf{v}_{n_i} - (\mathbf{v}_t + \mathbf{C}_{\mathrm{BI}}(\mathbf{q})^{\mathrm{T}}\boldsymbol{\omega}^{\times}\chi_i)]^{\mathrm{T}}\dfrac{\mathbf{L}_i}{\|\mathbf{L}_i\|}, & \text{for } \|\mathbf{L}_i\| - L_0 > 0 \\ 0, & \text{otherwise} \end{cases} \tag{30}$$

where $\mathbf{v}_t$ and $\mathbf{v}_{n_i}$ are the velocity components of the debris and junction in $\mathcal{F}_I$, respectively. The tether material is assumed to have a constant spring constant k and damping coefficient c calculated as previously discussed in Eqs. (16) and (17), respectively.

G. Equations of Motion

The equations of motion of the chaser spacecraft, debris, and tether can be broken down into two phases: deployment of the tether, and detumbling of the TSS.

To model the motion, all forces contributing to translational motion for each body are included in Eq. (13). As a result of the chaser and tether nodes modeled as point masses, rotational motion is only modeled for the debris using Eq. (4).

During the tether deployment phase, the resulting net force on the debris in $\mathcal{F}_I$ is only due to gravitational effects. It is given by

$$m_t\frac{\mathrm{d}\dot{\mathbf{r}}_t}{\mathrm{d}t} = \mathbf{F}_t = \mathbf{F}_g = -\frac{\mu m_t}{\|\mathbf{r}_t\|^3}\mathbf{r}_t \tag{31}$$

Similarly, torque imparted on the debris is calculated only through contributions by gravity-gradient effects defined in $\mathcal{F}_B$:

$$\boldsymbol{\tau}_t = \boldsymbol{\tau}_g = \frac{3\mu}{\|\mathbf{r}_t^b\|^5}\mathbf{r}_t^{b\times}\mathbf{J}\mathbf{r}_t^b \tag{32}$$

The chaser spacecraft will be affected by gravitational effects and an impulse force $\mathbf{F}_{\mathrm{impulse}}$ that occurs when the tether is deployed. When performing attitude adjustments, the chaser will be affected by the thrust force $\mathbf{F}_{\mathrm{thrust}}$. Although these forces are conditional, together, they result in

$$\begin{aligned} m_c\frac{\mathrm{d}\dot{\mathbf{r}}_c}{\mathrm{d}t} &= \mathbf{F}_c = \mathbf{F}_g - \mathbf{F}_{\mathrm{impulse}} + \mathbf{F}_{\mathrm{thrust}} \\ &= -\frac{\mu m_c}{\|\mathbf{r}_c\|^3}\mathbf{r}_c - \sum_{i=1}^{4}\mathbf{F}_{\mathrm{impulse}_i}\frac{\mathbf{r}_b}{\|\mathbf{r}_b\|} + \mathbf{F}_{\mathrm{thrust}} \end{aligned} \tag{33}$$

A given tether node, denoted by the subscript i, experiences similar forces to the chaser before they are deployed from its surface as a result of being pulled by the proceeding node in the tether. A bullet will experience an additional one-time impulse force. These forces are given by the conditions

$$m_{n_i}\frac{\mathrm{d}\dot{\mathbf{r}}_{n_i}}{\mathrm{d}t}=\mathbf{F}_{n_i}=\begin{cases}\mathbf{F}_c, & \text{when } i \text{ is attached to the chaser}\\ \mathbf{F}_{g_i}+\mathbf{F}_{ii+1}+\mathbf{F}_{ii-1}, & \text{when } i \text{ is a tether node in flight}\\ \mathbf{F}_{g_i}+\sum_{k=1}^{4}\mathbf{F}_{is_{k_1}}+\mathbf{F}_{im_{\text{end}}}, & \text{when } i \text{ is the junction node in flight}\\ \mathbf{F}_{g_i}+\mathbf{F}_{ii-1}+\mathbf{F}_{\text{impulse}}, & \text{when } i \text{ is a bullet node in flight}\end{cases} \tag{34}$$

where the subscript s denotes the subtether, and m denotes the main tether.

During the postcapture stabilization phase, the resulting net force on the debris in $\mathcal{F}_I$ is due to the tension forces generated in the four subtethers and the gravitational effects. It is given by

$$m_t\frac{\mathrm{d}\dot{\mathbf{r}}_t}{\mathrm{d}t}=\mathbf{F}_t=\mathbf{F}_s+\mathbf{F}_g=\sum_{i=1}^{4}F_i\frac{\mathbf{L}_i}{\|\mathbf{L}_i\|}-\frac{\mu m_t}{\|\mathbf{r}_t\|^3}\mathbf{r}_t \tag{35}$$

When performing attitude adjustments, the chaser spacecraft will be affected by the thrust force $\boldsymbol{F}_{\text{thrust}}$. This results in

$$m_c\frac{\mathrm{d}\dot{\mathbf{r}}_c}{\mathrm{d}t}=\mathbf{F}_c=-\mathbf{F}_m+\mathbf{F}_g+\mathbf{F}_{\text{thrust}}=-F_m\frac{\mathbf{L}_m}{\|\mathbf{L}_m\|}-\frac{\mu m_c}{\|\mathbf{r}_c\|^3}\mathbf{r}_c+\mathbf{F}_{\text{thrust}} \tag{36}$$

where F_m denotes the force magnitude present in the main tether, and $\mathbf{L}_m$ denotes its vector components. The junction experiences similar forces:

$$m_j\frac{\mathrm{d}\dot{\mathbf{r}}_j}{\mathrm{d}t}=\mathbf{F}_j=\mathbf{F}_m-\mathbf{F}_s+\mathbf{F}_g=F_m\frac{\mathbf{L}_m}{\|\mathbf{L}_m\|}-\sum_{i=1}^{4}F_i\frac{\mathbf{L}_i}{\|\mathbf{L}_i\|}-\frac{\mu m_j}{\|\mathbf{r}_j\|^3}\mathbf{r}_{n_i} \tag{37}$$

Torque imparted on the debris is calculated as the sum of the four subtether contributions and the gravity-gradient effects defined in $\mathcal{F}_B$:

$$\boldsymbol{\tau}_t=\boldsymbol{\tau}_s+\boldsymbol{\tau}_g=\mathbf{C}_{\text{BI}}(\mathbf{q})\sum_{i=1}^{4}F_i\frac{\boldsymbol{\chi}_i^{\times}\mathbf{L}_i}{\|\mathbf{L}_i\|}+\frac{3\mu}{\|\mathbf{r}_t^b\|^5}\mathbf{r}_t^{b\times}\mathbf{J}\mathbf{r}_t^b \tag{38}$$

To summarize, to simulate the dynamics, Eqs. (35–38) are solved numerically with Eqs. (4) and (13).

III. On-Orbit Capture Simulation Results

The equations of motion and the tether numerical models presented in Sec. III are used to build upon Hovell and Ulrich's [23] work to examine the deployment dynamics of the novel tether configuration and create a complete end-to-end tether deployment and debris detumbling scenario. That is, the specific simulation setup used by Hovell and Ulrich [23] is recreated and built upon to join the tether deployment phase presented in this work and their postcapture detumbling phase work into a single simulation. The purpose of this simulation is to demonstrate the novel tether design in an appropriate missionlike environment: one which cannot be easily recreated under laboratory conditions. This section presents the orbital simulation results of the complete capture scenario.

The debris is modeled as a rectangular prism, and the chaser is modeled as a point mass. Two separate simulations are performed over one orbital period and combined together in order to achieve the full deployment and capture scenario. In the first simulation the tether deployment is simulated up until the point of contact between the tether bullets and the debris. In the second simulation, the chaser and target debris are simulated while connected by the tether for the remainder of the orbital period. The same initial orbital elements of the debris as used by Hovell and Ulrich [23] are defined in Table 1.

For use in the simulation, the target and chaser initial positions $\mathbf{R}$ and velocities $\mathbf{V}$ in $\mathcal{F}_I$ are required. These are calculated using the orbital elements found in Table 1. First, the magnitude of the radius vector R is calculated:

$$R=\frac{a(1-e^2)}{1+e\cos\theta} \tag{39}$$

Then, using this magnitude, the position and velocity vector components in the perifocal reference frame $\mathcal{F}_p$ are calculated as

$$\mathbf{R}_p=\begin{bmatrix}R\cos\theta\\ R\sin\theta\\ 0\end{bmatrix} \tag{40}$$

$$\mathbf{V}_p=\begin{bmatrix}-\sqrt{\dfrac{\mu}{a(1-e^2)}}\sin\theta\\ \sqrt{\dfrac{\mu}{a(1-e^2)}}(e+\cos\theta)\\ 0\end{bmatrix} \tag{41}$$

where μ is the gravitational parameter of the Earth. The $\mathbf{R}_p$ and $\mathbf{V}_p$ vectors are then rotated into $\mathcal{F}_I$ through the rotation matrix:

$$\mathbf{C}_{IP}=\begin{bmatrix}\cos\Omega\cos\omega-\sin\Omega\cos i\sin\omega & -\cos\Omega\sin\omega-\sin\Omega\cos i\cos\omega & \sin\Omega\sin i\\ \sin\Omega\cos\omega+\cos\Omega\cos i\sin\omega & -\sin\Omega\sin\omega+\cos\Omega\cos i\cos\omega & -\cos\Omega\sin i\\ \sin i\sin\omega & \sin i\cos\omega & \cos i\end{bmatrix} \tag{42}$$

which is used to obtain $\mathbf{R}_I$ and $\mathbf{V}_I$ of the target:

Table 1 Debris orbital elements used to define initial orbit of the complete capture scenario simulation

Orbital element	Value
Semimajor axis, a	6871 km
Eccentricity, e	0.001
Right ascension of the ascending node, Ω	20 deg
Inclination i	60 deg
Argument of perigee ω	90 deg
True anomaly θ_t	60 deg

$$\mathbf{R}_{I_t} = \mathbf{C}_{IP}\mathbf{R}_P = \begin{bmatrix} -6176 \\ -421 \\ 2974 \end{bmatrix} \text{km} \tag{43}$$

$$\mathbf{V}_{I_t} = \mathbf{C}_{IP}\mathbf{V}_P = \begin{bmatrix} -2.46 \\ -4.40 \\ -5.71 \end{bmatrix} \text{km/s} \tag{44}$$

The initial position and velocity vectors of the chaser spacecraft are similarly calculated; however, its position trails the target by 30 m in the flight direction. All orbital elements between the chaser and target debris are the same, with the exception of the chaser's true anomaly given as

$$\theta_c = \theta_t - \frac{30}{\|\mathbf{R}_{I_t}\|} \tag{45}$$

The simulations are performed using an Adams integration scheme over 5668 s. The tether bullets are deployed, each at a unique normalized vector $\boldsymbol{d}_i$, from the chaser so that they radiate outward from the chaser. The subscript i denotes the bullet number. Simulation parameters are found in Table 2.

Table 2 Initial conditions and parameters of the on-orbit tether deployment simulation

Parameter	Value
J_{xx}, kg · m^2	15,000
J_{yy}, kg · m^2	3,000
J_{zz}, kg · m^2	15,000
k, N/m	3,150
c, (N · s)/m	16
L_{main}, m	15.0
L_{sub}, m	15.2
v_b, m/s	0.08
m_t, kg	3,000
m_c, kg	500
m_n, kg	1
m_b, kg	5
m_j, kg	10
β	0.3025
γ	0.6000
No. of nodes/tether	5
$\boldsymbol{d}_1$	[0.9182, 0.0193, 0.3957]
$\boldsymbol{d}_2$	[0.9318, 0.0196, 0.3625]
$\boldsymbol{d}_3$	[0.9182, −0.0193, 0.3957]
$\boldsymbol{d}_4$	[0.9318, −0.0196, 0.3625]
Debris size, m	[1.25,1.75,1.25]
$\mathbf{q}_t$	[0.2113, −0.4532, 0.8627, 0.0755]
$\boldsymbol{\omega}_t$, rad/s	[0.0250, 0.0250, 0.0250]

Table 3 Initial conditions and parameters of the on-orbit postcapture simulation

Initial condition	Value
Debris attitude $\mathbf{q}_t$	[0.4083, 0.3169, −0.8558, −0.0213]
Debris angular rate $\boldsymbol{\omega}_t$	[−0.0096, 0.0252, 0.0341] rad/s
Debris position $\mathbf{R}_{I_t}$	[−6547, −1970, 6720] km
Debris velocity $\mathbf{V}_{I_t}$	[0.47, −3.85, −6.55] km/s
Chaser position $\mathbf{R}_{I_c}$	[−6547, −1970, 6720] km
Chaser velocity $\mathbf{V}_{I_c}$	[0.47, −3.85, −6.55] km/s
Tether junction position $\mathbf{R}_{I_j}$	[−6547, −1970, 6720] km
Tether junction velocity $\mathbf{V}_{I_j}$	[0.47, −3.85, −6.55] km/s
Bullet 1 attachment χ_1	[0.625, −0.875, 0.000] m
Bullet 2 attachment χ_2	[0.000, −0.875, 0.625] m
Bullet 3 attachment χ_3	[−0.625, −0.875, 0.000] m
Bullet 4 attachment χ_4	[0.000, −0.875, −0.625] m

Upon contact with the debris, the final deployment simulation values as seen in Table 3 are saved and used as the initial conditions of the detumbling simulation. The detumbling simulation is run for the remainder of the orbital period. The values used as the detumbling simulation initial conditions are both the chaser and debris positions and velocities, the debris attitude and angular rates, and the four contact points of the tether bullets with the debris in $\mathcal{F}_B$. The bullet contact points with the debris were found to have negligible differences between both the spring–damper and ANCF simulations. As a result, one set of attachment points is used.

In the complete capture scenario, the tether is deployed from the chaser and stretches to its maximum unstretched length; at which point, contact between the debris and tether is made, and the detumbling phase begins. Once detumbling, the chaser continually thrusts in the retrograde direction with a force of 20 N to maintain tension on the tether. Figures 2a and 2b depict the novel tether configuration deployment using the spring–damper model, whereas Figs. 2c and 2d depict tether deployment using the ANCF model. Tether deployment takes place over 370 s. Figure 2e shows the immediate TSS configuration postcapture. All on-orbit simulation figures are displayed using a fixed inertial frame.[‡]

Figure 3 shows the results of the postcapture stabilization process over the remainder of the orbital period, given the initial conditions found in Table 3. Figure 3a shows the debris angular rates settling, Fig. 3b shows the tether equilibrium angle approaching zero, and Fig. 3c shows the tether elongation diminishing over time. These results are consistent with Hovell and Ulrich's [23] findings, and they demonstrate the passive stabilization properties of the subtether configuration are still present in a complete capture scenario. From these results, it is concluded that the novel tether configuration is capable of deploying nominally in an orbital environment, contacting tumbling debris, and passively reducing its angular velocity over time.

IV. Experimental Validation of Numerical Models

This section presents the experimental validation of both numerical tether models and the complete capture scenario.

A. Tether Deployment Validation

To experimentally validate both numerical tether models, a tether deployment apparatus was designed and assembled for use with the Spacecraft Proximity Operations Testbed (SPOT), which is housed within Carleton University's Spacecraft Robotics and Control Laboratory. The SPOT consists of a smooth granite surface mounted on a steel frame. Two identical platforms are used on this surface to simulate spacecraft. They float using air bearings that expel air downward, creating a thin film of air between themselves and the surface. This floating process is near friction free and allows the platforms to emulate

[‡]A video of the complete capture scenario can be accessed at https://tinyurl.com/yy9faazm [retrieved 26 November 2019].

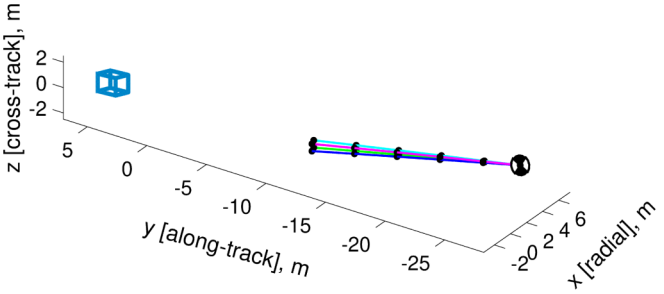

a) Spring–damper model tether deployment 3% through orbit

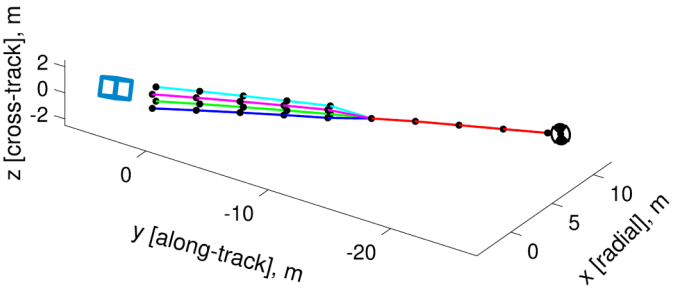

b) Spring–damper model tether deployment 6% through orbit

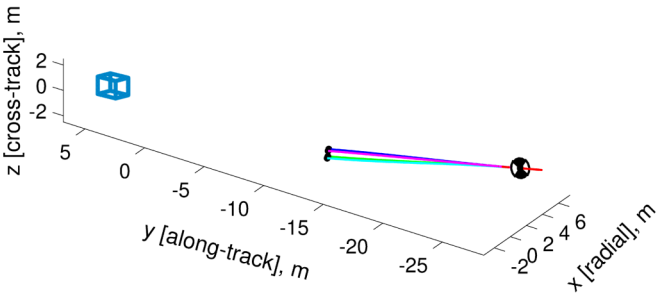

c) ANCF model tether deployment 3% through orbit

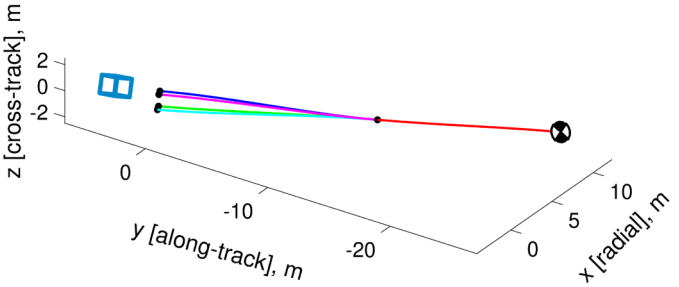

d) ANCF model tether deployment 6% through orbit

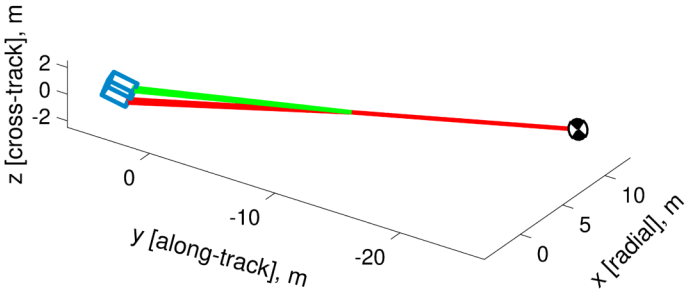

e) Initial position of the TSS postcapture

Fig. 2 Novel tether configuration deployment and contact in an orbital environment.

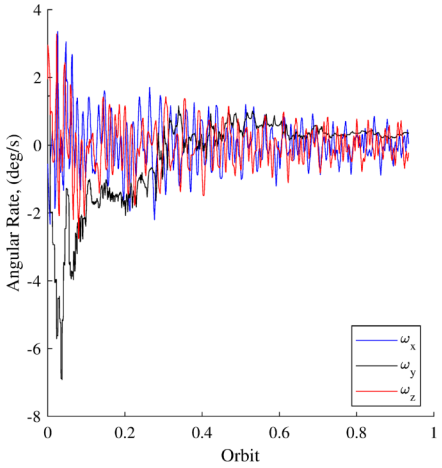

a) Debris angular rates

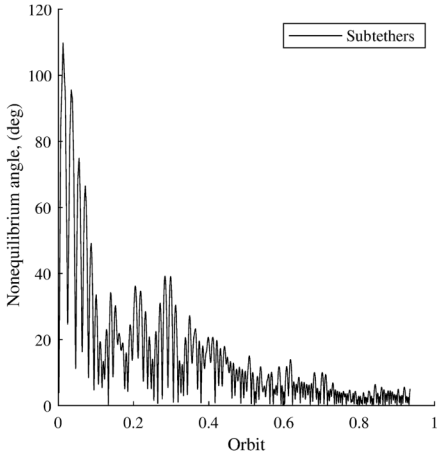

b) Tether angle

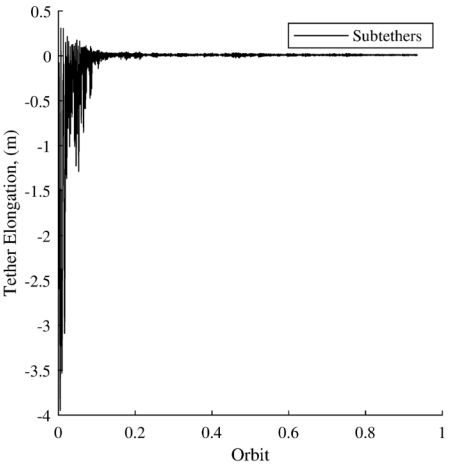

c) Tether elongation

Fig. 3 Detumbling motion of the tethered-spacecraft system.

deep space movement within a plane of motion. Planar translational and rotational motion is achieved using eight air nozzles located on the four sidewalls of each platform. The red platform acts as the chaser spacecraft, and the black platform acts as the debris. Figure 4a shows an overview of the SPOT facility, and Fig. 4b shows the two SPOT platforms used for experimental validation.

Contrary to the simulated tether deployment shown in Fig. 1b, the experiment only uses a tether with two bullets and two subtethers. This is due to the planar restrictions of the SPOT. The tether deployment apparatus uses compressed air to propel two tether bullets forward. The air is contained in a 3000 psi tank and regulated to 250 psi using a high-pressure regulator. A normally closed solenoid

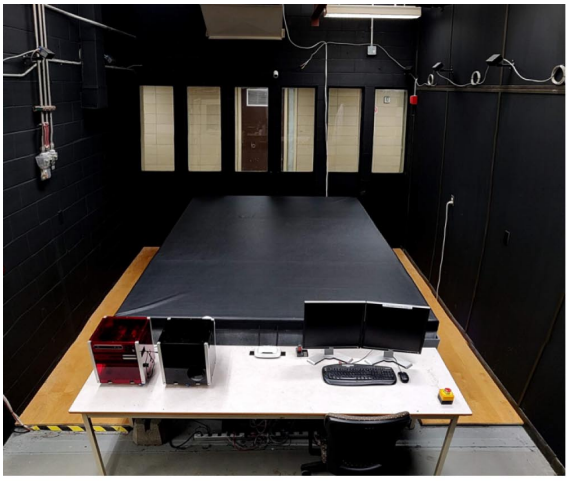

a) Overview of the spacecraft proximity operations test bed

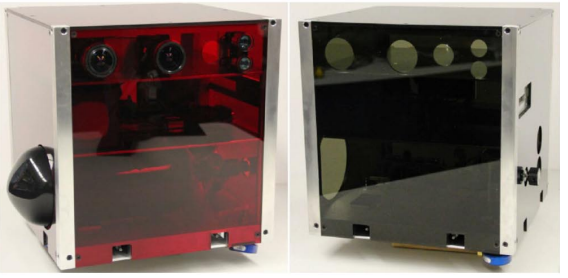

b) SPOT platforms

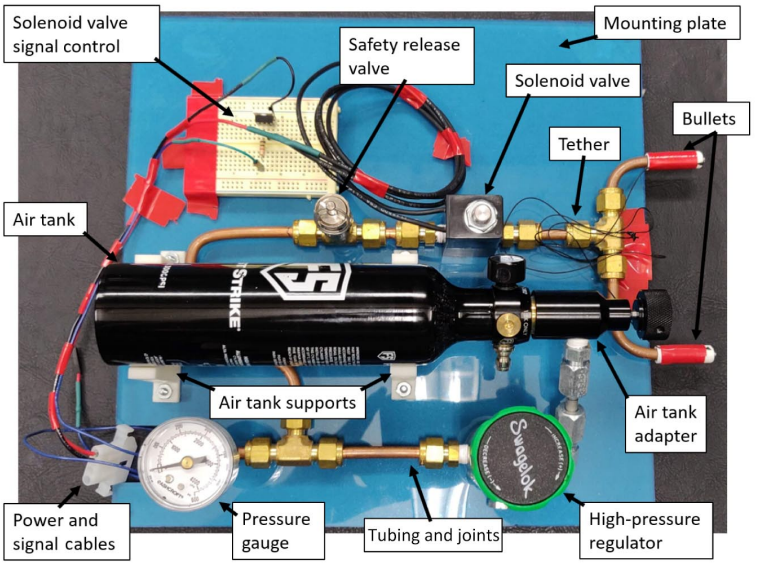

c) Tether deployment apparatus installed on chaser platform

Fig. 4 Experimental laboratory and apparatuses.

valve is connected to a Raspberry Pi 3 controller on board the SPOT platform. It is opened at the time of deployment, allowing air to travel through the copper piping and exit the system, propelling the bullets forward. The bullets have a metal tip and contact with a magnetic plate mounted on the side of the debris SPOT platform in order to establish a tethered connection. The tether deployment apparatus with labeled components is seen in Fig. 4c.

The tether deployment and capture experiment was performed on the SPOT for a total of 16 s. Figure 5a shows the initial positions of the two platforms. During the initial 15 s of the experiment, the debris platform rotates in place to simulate how a debris may arbitrary rotate as it drifts in space. The chaser platform orbits around the debris in an anticlockwise circular motion, always facing it and maintaining one tether length of distance between the two platforms. This scenario is chosen to create a differential in angular velocity between the two platforms, thereby emulating a nonideal pose tracking maneuver. When an opportunity for tether deployment is available (that is, a suitable surface on the debris platform is aligned with the chaser), the tether is deployed. As seen in Fig. 5b, tether deployment occurs when the chaser is roughly at the position (1,1) m on the table and the tether deployment payload and debris platform impact panel are aligned. Deployment lasts 1 s.

The tether deployment scenario was numerically simulated in a planar environment replicating the conditions of the SPOT using both the spring–damper and ANCF models. The same method as the on-orbit simulations was followed, with the restriction that translation motion could only happen in the x and y axes and rotation about the z axis. These restrictions created a three-degree-of-freedom environment, as opposed to the six-degree–of-freedom orbital environment. Table 4 contains the experimental and simulation parameters used.

Figure 6 shows key frames of the experiment. Figures 6a and 6b show the spring–damper model at 0.5 and 1.0 s, respectively; whereas Figs. 6d and 6e show the ANCF simulation at 0.5 and 1.0 s, respectively. The tethers immediately postcontact are seen in Figs. 6c and 6f. Tether nodes are represented by black dots, whereas connecting elements are shown using gray lines (see footnote 1).

Ten tether deployment experiments were performed and recorded using a slow-motion camera. Node locations were marked on the tether, and their positions were manually recorded at 0.1 s intervals of the experiment. A calibration between camera pixels and SPOT table location was performed to overlay the experimental nodes with the simulation node positions to visualize the accuracy of the simulation. Figure 7 shows a single frame as an example of this comparison of tether node positions. Figures 8a–8c show the displacement of the two subtether and junction nodes during their deployment for each tether model.

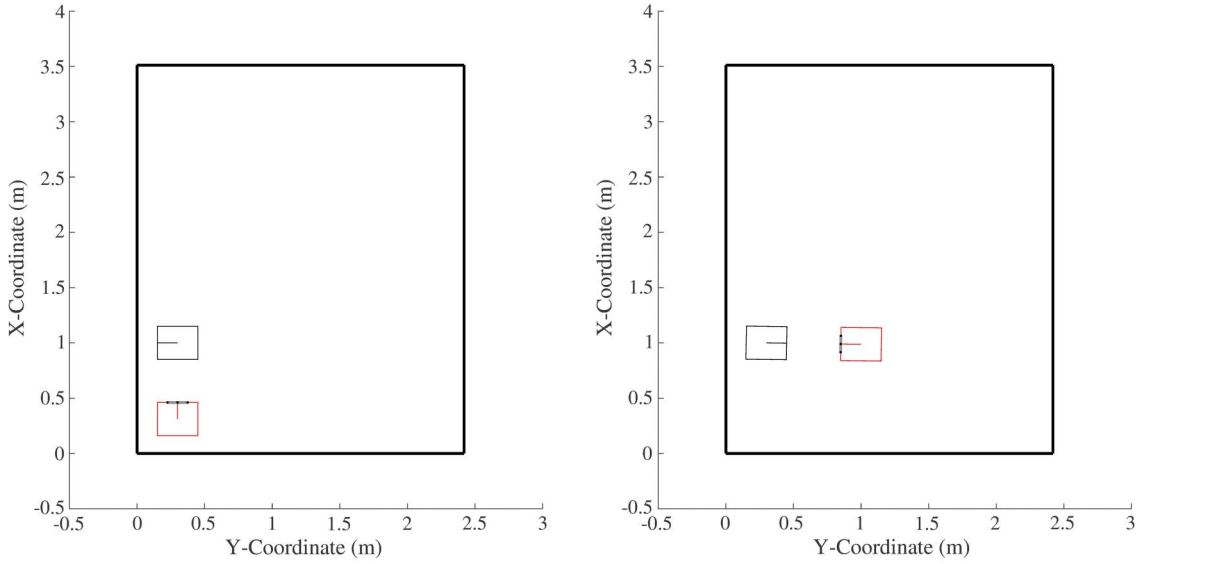

a) Simulated platform initial positions

b) Simulated platform locations at the time of tether deployment

Fig. 5 Experimental scenario SPOT platform movement.

To quantify the errors between the experimental tether node positions and the simulated tether node positions, the absolute residual of the tether nodes is used. This is expressed as

$$\boldsymbol{re}_i = |\boldsymbol{s}_i - \boldsymbol{ex}_i| \tag{46}$$

where $\boldsymbol{s}_i$ and $\boldsymbol{ex}_i$ represent the displacement of the ith tether node in simulation and experiment, respectively.

For each time step of each experiment, the absolute residual of each tether node and the junction node is calculated. For conciseness, only the absolute residuals of a single experiment trial are shown in the box plots of Fig. 9.

The absolute residuals of each node, for each model, averaged across all 10 experiments are shown in Table 5.

Overall, the average absolute residual of every node for both the spring–damper and ANCF models lies at only a few centimeters of error. The total deployment length in the x axis is a constant 58, whereas the y axis varies but has an average displacement of 5. As seen in Table 5, on average, the spring–damper model error is less for the bullets and for the nodes close to the tip of the subtethers. The ANCF model error is less at the junction, the subtether nodes closest to it, and the main tether. The error found in the ANCF model is, on average, higher than that of the spring–damper model. This is explained due to artificial errors that are inherently introduced into the model. Indeed, each ANCF tether element must always remain its total unstretched length when no forces are acting on it. Due to this, when the endpoints of the tether are initially defined, the shape function at that state will dictate how the tether is folded. The ANCF shape function initially folds the tether along this axis and, in order to accommodate the full unstretched length of the tether, it will create an "S" shape. This contrasts with the spring–damper model and experimental tether, which are spooled into one single point and run along the edge of the platform in a straight line.

Table 4 Laboratory experiment parameters

Parameter	Value
A, m^2	7.85×10^{-7}
ρ, kg/m^3	1150
k, N/m	175
c, (N · s)/m	1.1
$F_{\text{deployment}}$, N	77
m_b, kg	1.50×10^{-3}
m_{tether}, kg	1.00×10^{-4}
m_{RED}, kg	21.23
m_{BLACK}, kg	13.75
L_{main}, m	0.28
L_{sub}, m	0.28
I_{RED}, kg/m^2	0.29
I_{BLACK}, kg/m^2	0.19

Table 5 Average relative residuals of the spring–damper and ANCF models

	Axis			
	x		y	
Model	S-D, cm	ANCF, cm	S-D, cm	ANCF, cm
		Node 1		
Subtether 1	3.09	3.46	1.45	1.31
Subtether 2	2.89	3.91	1.36	1.44
Main tether	2.25	1.27	0.40	0.59
		Node 2		
Subtether 1	2.92	3.04	1.52	1.82
Subtether 2	3.15	3.08	1.16	1.32
Main tether	2.14	1.36	0.36	0.53
		Node 3		
Subtether 1	2.88	3.39	1.69	2.19
Subtether 2	3.46	3.16	1.82	2.17
Main tether	1.36	1.00	0.30	0.32
		Node 4		
Subtether 1	2.92	3.32	1.75	1.96
Subtether 2	3.45	3.06	3.12	2.36
Main tether	0.60	0.49	0.20	0.12
		Node 5		
Subtether 1	2.75	2.68	1.72	0.97
Subtether 2	3.08	2.44	2.16	1.60
Main tether	0.00	0.00	0.00	0.00
		Junction Node		
	2.08	1.55	0.46	0.60

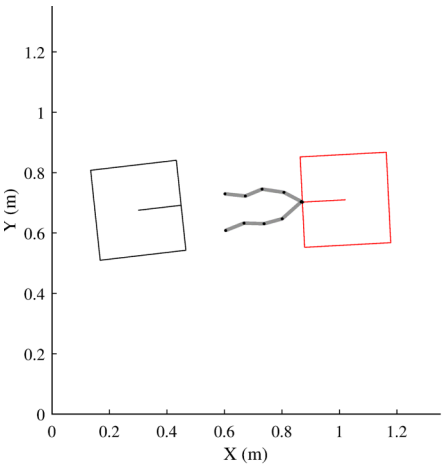

a) Planar spring–damper model tether deployment at 0.5 s

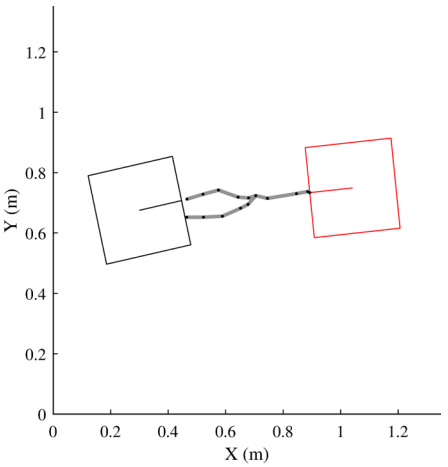

b) Planar spring–damper model tether deployment at 1.0 s

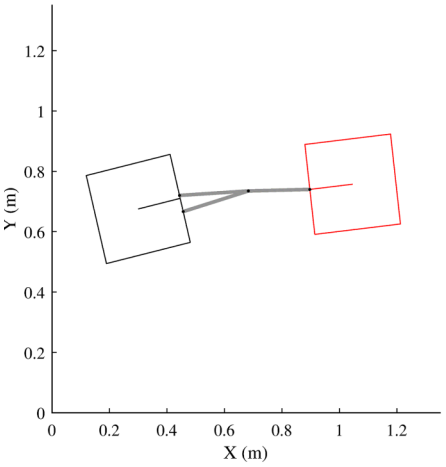

c) Initial position of the planar spring–damper model TSS postcapture at 1.1 s

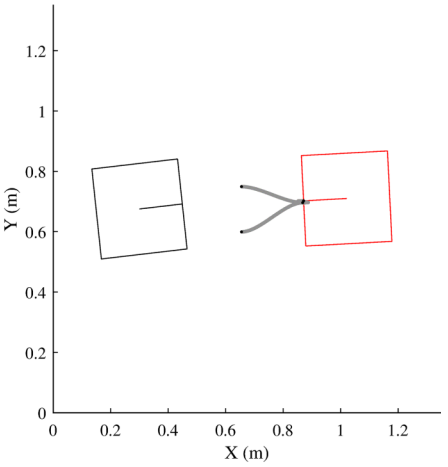

d) Planar ANCF model tether deployment at 0.5 s

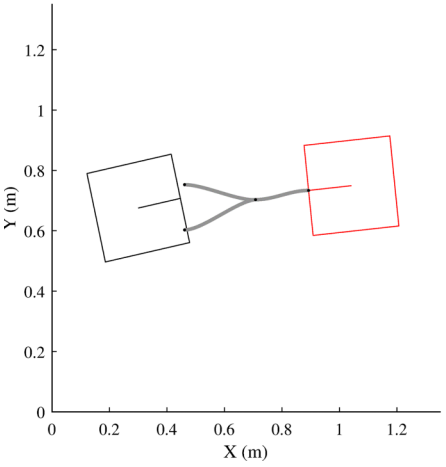

e) Planar ANCF model tether deployment at 1.0 s

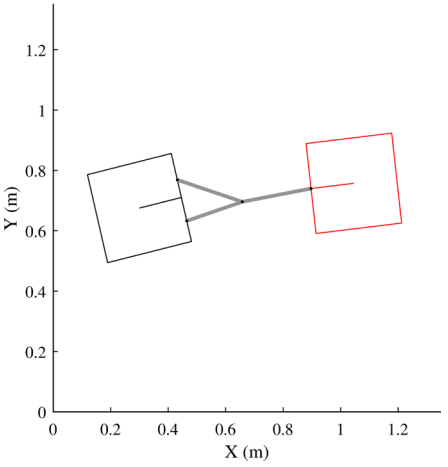

f) Initial position of the planar ANCF model TSS postcapture at 1.1 s

Fig. 6 Experimental results of novel tether configuration deployment in a planar environment using the massless spring–damper and ANCF models.

Other errors associated with the tether deployment experiment are air resistance and gravitational force acting in the z axis. Air resistance is not accounted for in the simulated planar environment because it is assumed to have a minimal effect on the tether dynamics due to their very small surface area. However, in practice, there will be a very small change in the tether dynamics due to the resisting force. In simulation, gravitational forces are not accounted for because the simulated planar environment does not have a third dimension for the force to act in. In experiment, the gravitational forces were found to cause the tether and bullets to drop in height by a few centimeters. The existence of a third dimension and constant force in experiment changes tether fight dynamics, but since the force

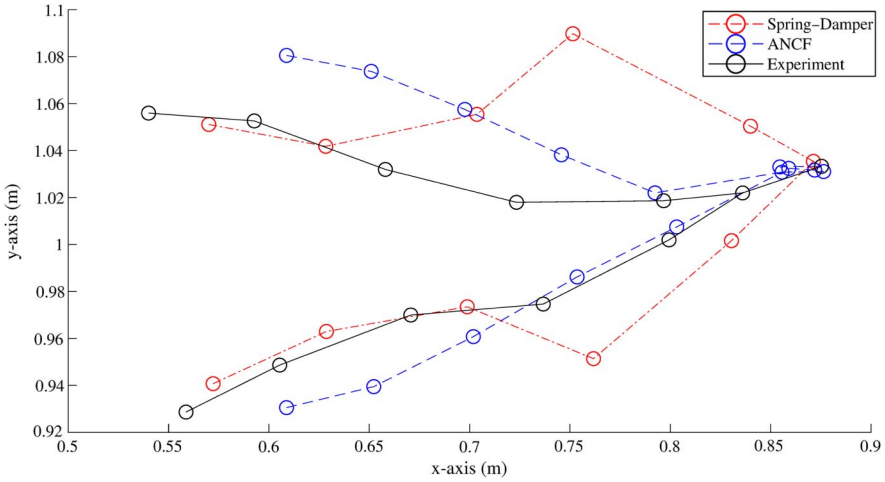

Fig. 7 Spring–damper, ANCF, and experimental tether node positions of experiment 3 at 0.6 s.

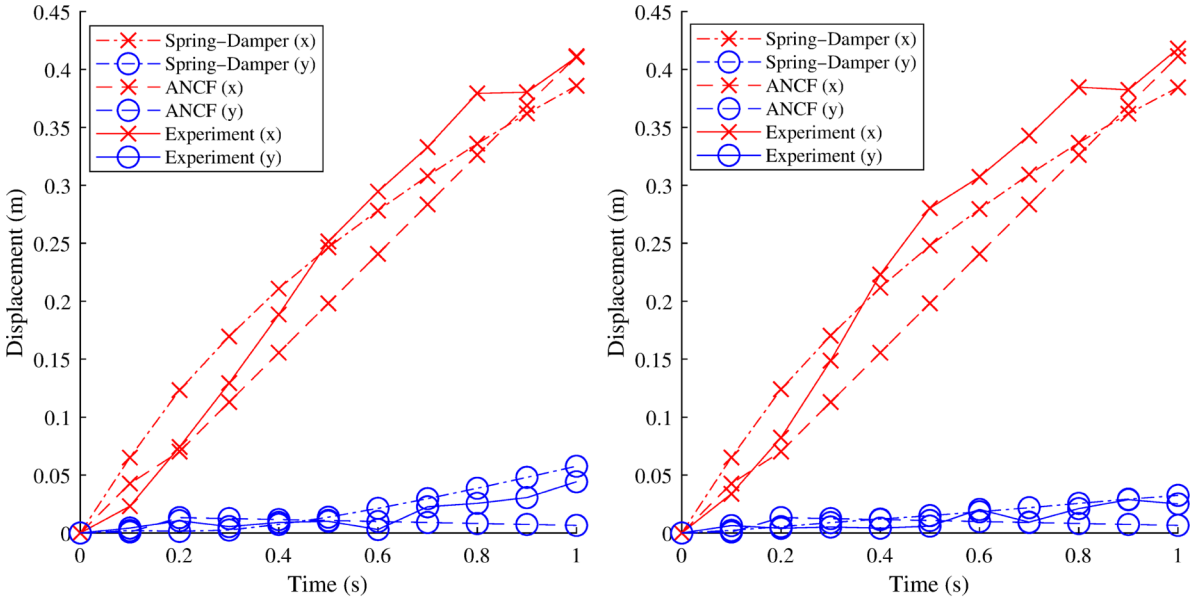

a) Experiment 3 subtether one-bullet node displacement

b) Experiment 3 subtether two-bullet node displacement

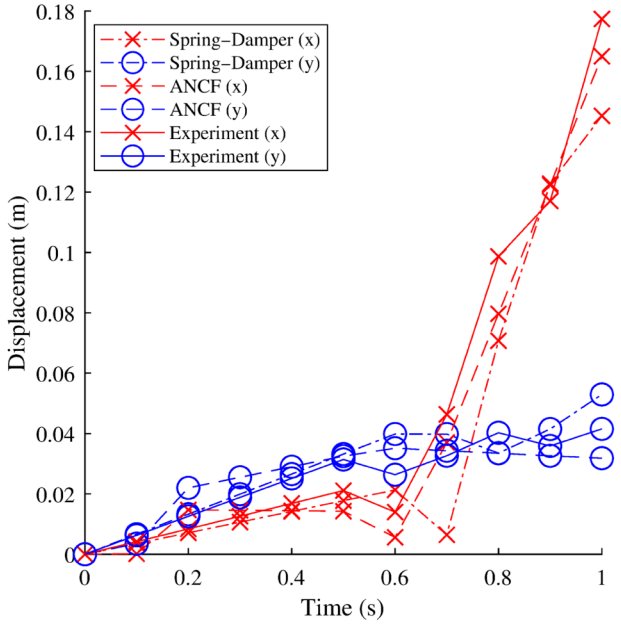

c) Experiment 3 junction node displacement

Fig. 8 Experimental results of novel tether configuration deployment in a planar environment using the massless spring–damper and ANCF models.

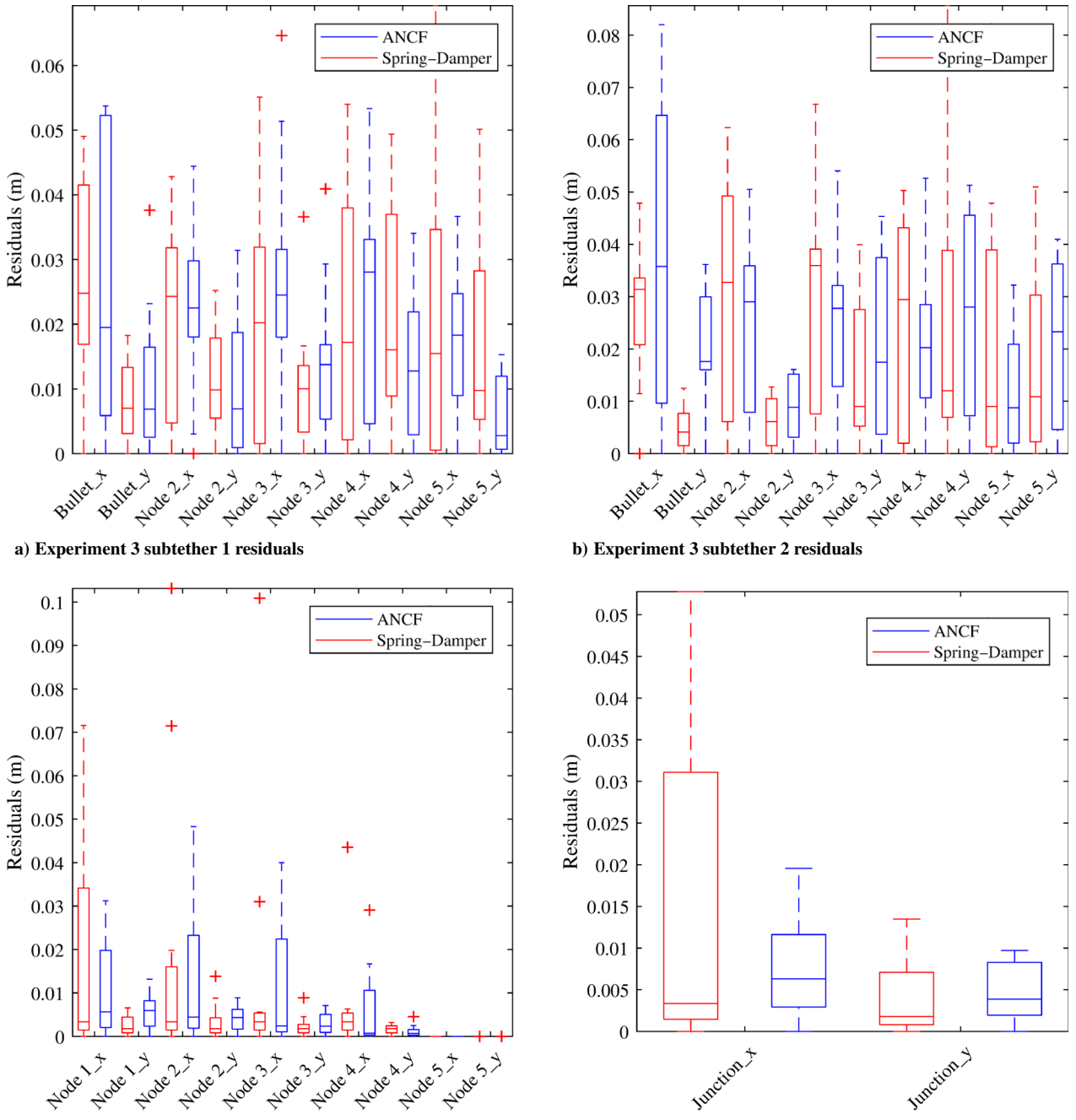

a) Experiment 3 subtether 1 residuals

b) Experiment 3 subtether 2 residuals

c) Experiment 3 main tether residuals

d) Experiment 3 junction residuals

Fig. 9 Experiment 3 individual tether node absolute residuals over the duration of tether deployment.

cannot be removed and affects the experiments equally, all results have the same induced error. Considering all of the errors, the average absolute residuals are found to be low and confirm that, although both numerical models are capable of describing the motion of the experimental tethers, the spring–damper model is better at describing the motion of the tether ends and nodes closest to them, whereas the ANCF model is better at describing the motion of the junction, nearby nodes, and the main tether.

B. Planar Complete Capture Scenario

To demonstrate the complete capture scenario in a planar environment, the experimental trajectories of the red "chaser", labeled RED, and black "debris", labeled BLACK, platforms are compared to their simulated counterparts. During the postcapture segment, the attachment points between both subtether bullets and the debris platform are the same as shown in Figs. 6c and 6f. Platform positions and pointing angles are shown in Fig. 10.

Figures 10a and 10c show the platform positions, whereas Figs. 10b and 10d show the wrapped platform pointing angles. Experimental trajectories are are denoted by lines labeled "Exp", simulated platform trajectories using the ANCF tether model are represented by lines labeled "ANCF Sim", and simulated platform trajectories using the spring-damper tether model are represented by lines labeled "S-D Sim". The experimental and simulation TSS platform trajectories have the same general direction of movement and pointing angles postcapture. However, beyond the similar motion, a sleight discrepancy can be seen between the experimental and simulation values when the subtethers are in tension, as seen during the 40–70 s time span of Figs. 10b and 10d. The angle that the debris achieves in simulation is much larger than in the experiment. This discrepancy was concluded to be due to several factors, including an

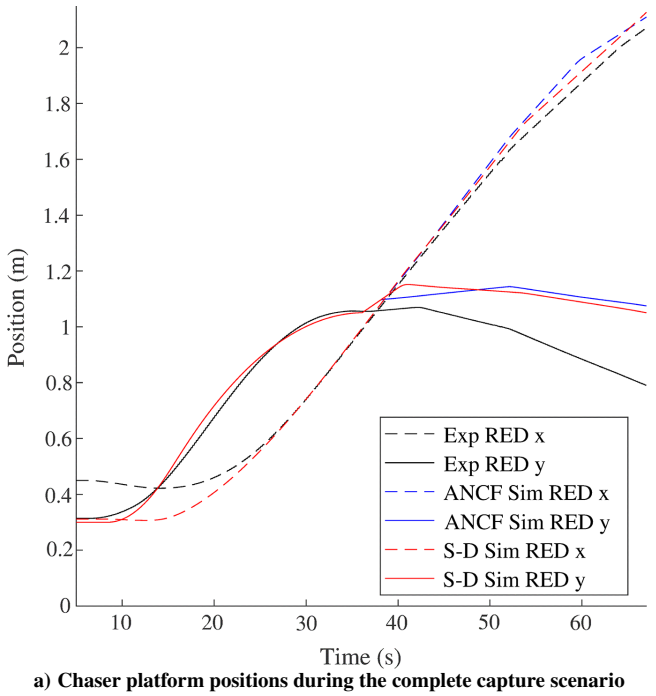

a) Chaser platform positions during the complete capture scenario

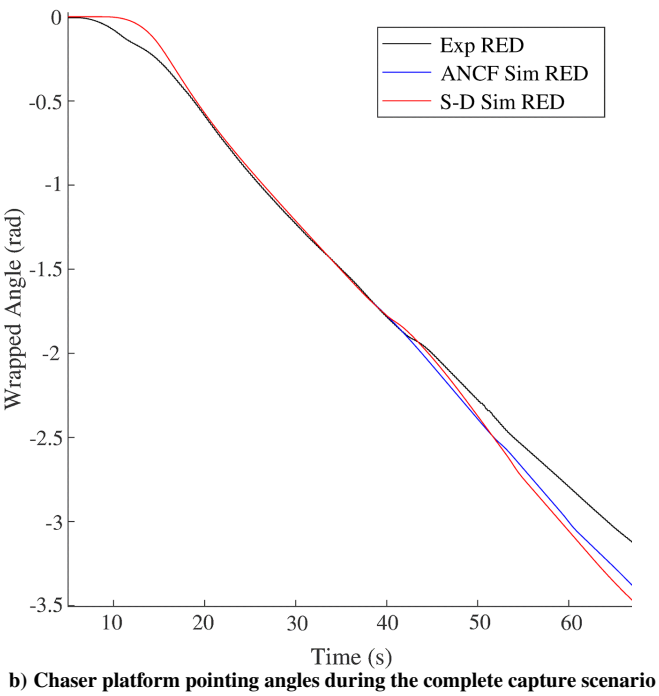

b) Chaser platform pointing angles during the complete capture scenario

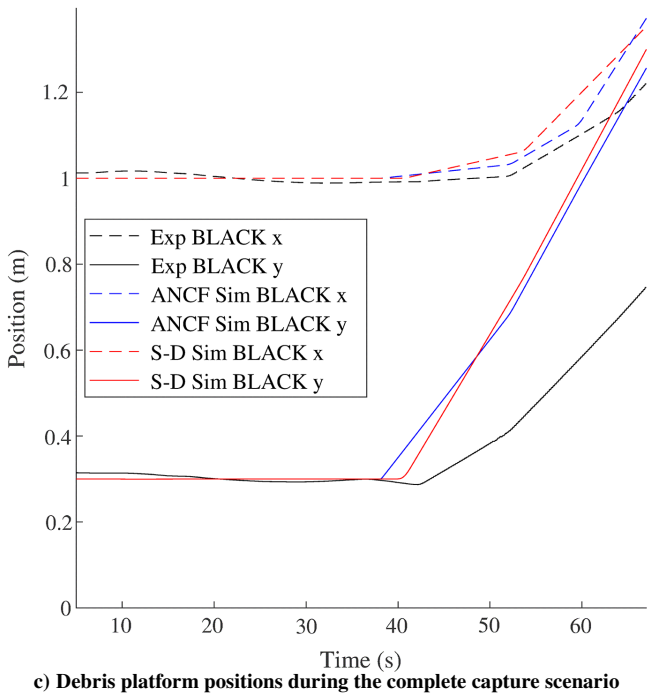

c) Debris platform positions during the complete capture scenario

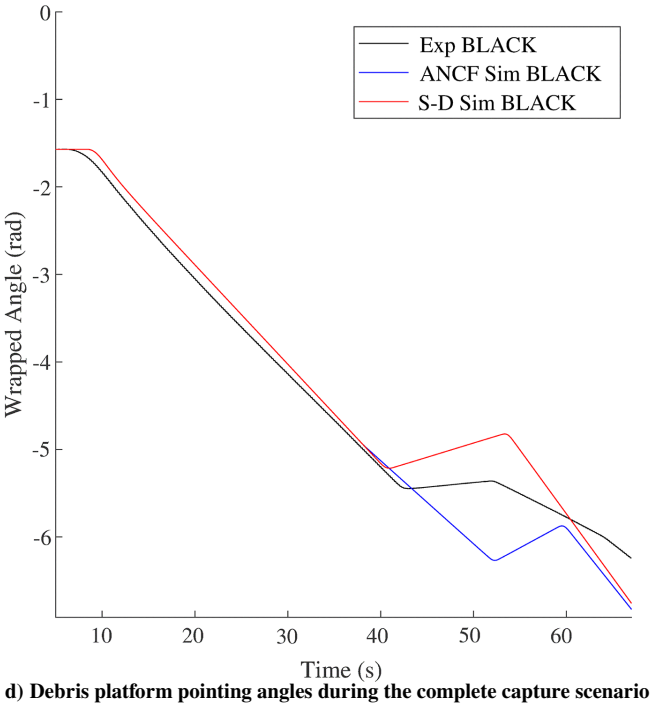

d) Debris platform pointing angles during the complete capture scenario

Fig. 10 Platform positions and pointing angles during the planar complete capture scenario.

imperfect experimentally determined spring constant and damping ratio of the tether, the platform velocities being lower than expected, air resistance on the platforms, and the tether not contacting at the maximum unstretched length.

The full experimental capture scenario was only run for 70 s due to the platforms approaching the limits of the table. A longer simulation that ignored the SPOT table boundaries was run to view the planar motion of the TSS over time. The simulation begins just before tether deployment and spends 60 s in the postcapture phase. Figures 11a and 11c show the TSS platform positions, whereas Figs. 11b and 11d show the wrapped pointing angles during this longer simulation. The pointing angle of the debris platform can be seen to dampen over time as the platforms rotate, confirming Hovell and Ulrich's [23] original findings (see footnote 1).

This experiment was performed to demonstrate, for the first time, a complete capture scenario of the tethering to uncooperative debris with differing angular rates using the novel tether configuration. It is concluded that a complete capture scenario in a planar environment using the novel tether configuration is possible.

V. Conclusions

A novel tether configuration for tethered-net-based orbital debris capture was numerically modeled using both a lumped mass node with a massless spring–damper element model and an absolute nodal coordinate formulation model. The deployment dynamics of these models was simulated and experimentally validated in a

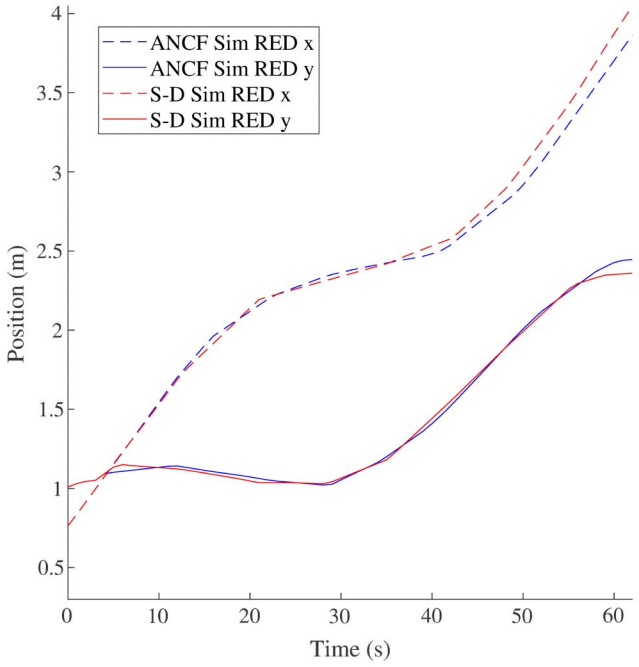

a) Chaser platform positions during the simulated longer complete capture scenario

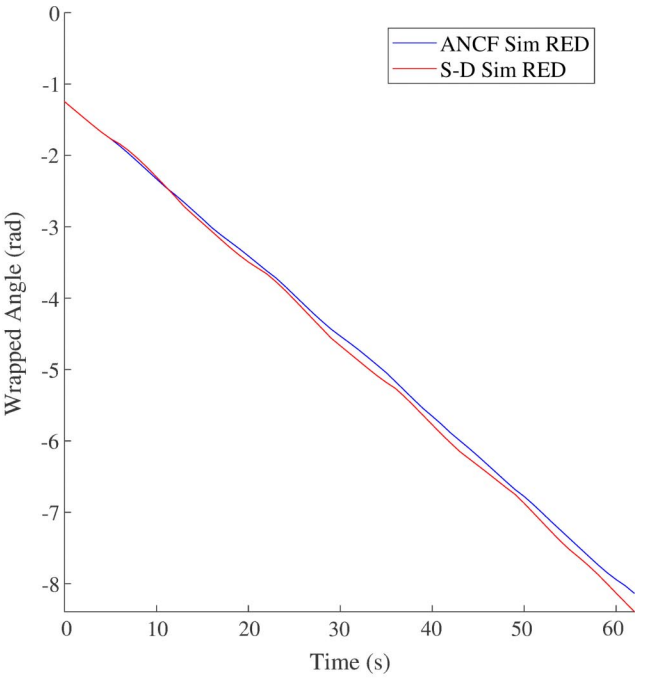

b) Chaser platform pointing angles during the simulated longer complete capture scenario

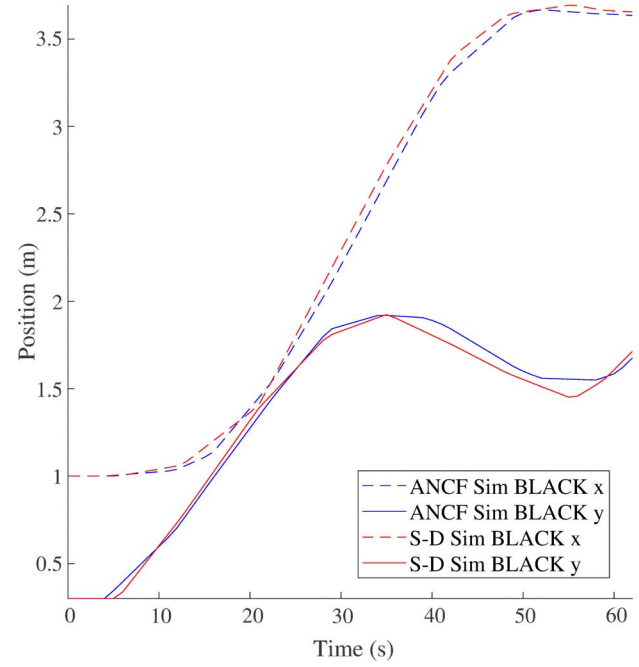

c) Debris platform positions during the simulated longer complete capture scenario

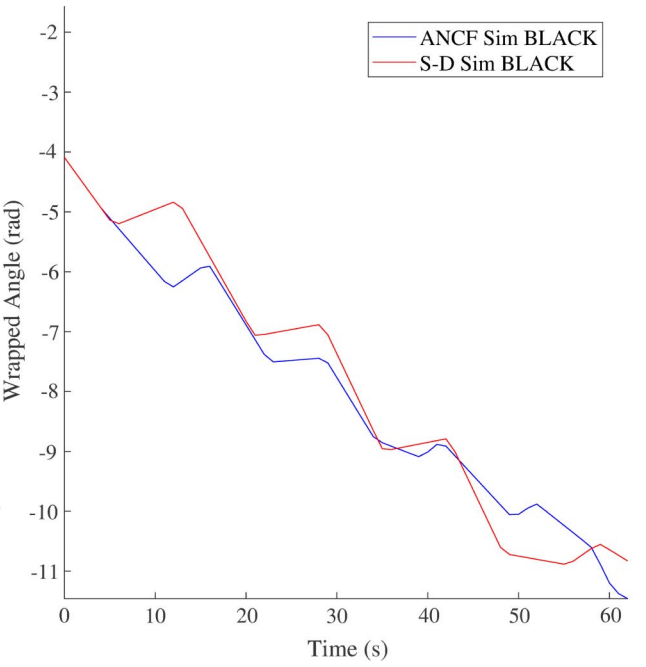

d) Debris platform pointing angles during the simulated longer complete capture scenario

Fig. 11 Platform positions and pointing angles during the longer simulated planar complete capture scenario.

planar environment. It is concluded that both models are adequate at describing the motion of the tethers during deployment. Specifically, the ANCF model is better at describing the motion of the junction and main tether element, as well as the overall tether once it has been mostly deployed. The spring–damper model is better at describing the motion of the bullets, subtether elements, and the early deployment motion of the overall tether. Lastly, a complete capture scenario using the novel tether configuration was presented in both planar and orbital environments for the first time. It was demonstrated that the novel tether configuration is capable of performing a complete capture and debris stabilization maneuver.

References

[1] Kessler, D. J., and Cour-Palais, B. G., "Collision Frequency of Artificial Satellites: The Creation of a Debris Belt," *Journal of Geophysical Research*, Vol. 83, No. A6, 1978, pp. 2637–2646. https://doi.org/10.1029/JA083iA06p02637

[2] Liou, J.-C., "An Active Debris Removal Parametric Study for LEO Environment Remediation," *Advances in Space Research*, Vol. 47, No. 11, 2011, pp. 1865–1876. https://doi.org/10.1016/j.asr.2011.02.003.

[3] Shan, M., Guo, J., and Gill, E., "Review and Comparison of Active Space Debris Capturing and Removal Methods," *Progress in Aerospace Sciences*, Vol. 80, Jan. 2016, pp. 18–32. https://doi.org/10.1016/j.paerosci.2015.11.001

[4] Wormnes, K., Le Letty, R., Summerer, L., Schonenborg, R., Dubois-Matra, O., Luraschi, E., Cropp, A., Krag, H., and Delaval, J., "ESA Technologies for Space Debris Remediation," *6th European Conference on Space Debris*, Vol. 1, ESA Communications ESTEC, Noordwijk, The Netherlands, 2013, pp. 1–8.

[5] Kaplan, M. H., Boone, B., Brown, R., Criss, T. B., and Tunstel, E. W., "Engineering Issues for All Major Modes of In Situ Space Debris Debris Capture," *AIAA Space 2010 Conference and Exposition*, AIAA Paper 2010-8863, 2010. https://doi.org/10.2514/6.2010-8863

[6] Wen, H., Jin, D. P., and Hu, H. Y., "Advances in Dynamics and Control of Tethered Satellite Systems," *Acta Mechanica Sinica/Lixue Xuebao*, Vol. 24, No. 3, 2008, pp. 229–241. https://doi.org/10.1007/s10409-008-0159-9

[7] Bonnal, C., Ruault, J. M., and Desjean, M. C., "Active Debris Removal: Recent Progress and Current Trends," *Acta Astronautica*, Vol. 85, April 2013, pp. 51–60. https://doi.org/10.1016/j.actaastro.2012.11.009

[8] Botta, E. M., Sharf, I., and Misra, A. K., "Contact Dynamics Modeling and Simulation of Tether Nets for Space-Debris Capture," *Journal of Guidance, Control, and Dynamics*, Vol. 40, No. 1, 2017, pp. 110–123. https://doi.org/10.2514/1.G000677

[9] Shan, M., "Net Deployment and Contact Dynamics of Capturing Space Debris Objects," Ph.D. Thesis, Delft Univ. of Technology, Delft, The Netherlands, 2018. https://doi.org/10.4233/uuid:803af7c5-4a97-48e9-870b-8e2f6fd325d8

[10] Benvenuto, R., Lavagna, M. R., and Salvi, S., "Multibody Dynamics Driving GNC and System Design in Tethered Nets for Active Debris Removal," *Advances in Space Research*, Vol. 58, No. 1, 2016, pp. 45–63. https://doi.org/10.1016/j.asr.2016.04.015

[11] Botta, E. M., Sharf, I., Misra, A. K., and Teichmann, M., "On the Simulation of Tether-Nets for Space Debris Capture with Vortex Dynamics," *Acta Astronautica*, Vol. 123, June 2016, pp. 91–102. https://doi.org/10.1016/j.actaastro.2016.02.012

[12] Shan, M., Guo, J., and Gill, E., "Deployment Dynamics of Tethered-Net for Space Debris Removal," *Acta Astronautica*, Vol. 132, March 2017, pp. 293–302. https://doi.org/10.1016/j.actaastro.2017.01.001

[13] Zhao, Y., Huang, P., and Zhang, F., "Capture Dynamics and Net Closing Control for Tethered Space Net Robotics," *Journal of Guidance, Control, and Dynamics*, Vol. 42, No. 1, 2019, pp. 199–208. https://doi.org/10.2514/1.G003672.

[14] Lavagna, M. R., Armellin, R., Bombelli, A., Benvenuto, R., and Carta, R., "Debris Removal Mechanism Based on Tethered Nets," *International Symposium on Artificial Intelligence, Robotics and Automation in Space*, Turin, Italy, 2012, pp. 1–6.

[15] Cercos, L., Stefanescu, R., Medina, A., Benvenuto, R., Lavagna, M., Gonzalez, I., Rodriguez, N., and Wormnes, K., "Validation of a Net Active Debris Removal Simulator Within Parabolic Flight Experiment," *International Symposium on Artificial Intelligence, Robotics and Automation in Space*, Montreal, QC, Canada, 2014, pp. 1–8.

[16] Medina, A., Cercòs, L., Stefanescu, R., Benvenuto, R., Lavagna, M., Gonzalez, I., Rodriguez, N., and Ormnes, K., "Capturing Nets for Active Debris Removal: A Follow-Up on Microgravity Experiment Design To Validate Flexible Dynamic Models," *13th Symposium on Advanced Space Technologies in Automation and Robotics*, Noordwijk, The Netherlands, 2015, pp. 1–8.

[17] Gołębiowski, W., Michał, D., Battista, U., and Wormnes, K., "Validation of Flexible Bodies Dynamics Simulator in Parabolic Flight," *Acta Astronautica*, Vol. 129, Dec. 2016, pp. 229–240. https://doi.org/10.1016/j.actaastro.2016.08.037

[18] Forshaw, J. L., Aglietti, G. S., Navarathinam, N., Kadhem, H., Salmon, T., Pisseloup, A., Joffre, E., Chabot, T., Retat, I., Axthelm, R., Barraclough, S., Ratcliffe, A., Bernal, C., Chaumette, F., Pollini, A., and Steyn, W. H., "RemoveDEBRIS: An In-Orbit Active Debris Removal Demonstration Mission," *Acta Astronautica*, Vol. 127, Oct. 2016, pp. 448–463. https://doi.org/10.1016/j.actaastro.2016.06.018

[19] Aslanov, V. S., and Yudintsev, V. V., "Dynamics of Large Space Debris Removal Using Tethered Space Tug," *Acta Astronautica*, Vol. 91, Oct. 2013, pp. 149–156. https://doi.org/10.1016/j.actaastro.2013.05.020

[20] Hovell, K., and Ulrich, S., "Attitude Stabilization of an Unknown and Spinning Target Spacecraft Using a Visco-Elastic Tether," *13th Symposium on Advanced Space Technologies in Robotics and Automation*, Noordwijk, The Netherlands, 2015, pp. 1–8.

[21] Hovell, K., and Ulrich, S., "Attitude Stabilization of an Uncooperative Spacecraft in an Orbital Environment Using Visco-Elastic Tethers," *AIAA Guidance, Navigation, and Control Conference*, AIAA Paper 2016-0641, 2016. https://doi.org/10.2514/6.2016-0641

[22] Hovell, K., and Ulrich, S., "Experimental Validation for Tethered Capture of Spinning Space Debris," *AIAA Guidance, Navigation, and Control Conference*, AIAA Paper 2017-1049, 2017. https://doi.org/10.2514/6.2017-1049

[23] Hovell, K., and Ulrich, S., "Postcapture Dynamics and Experimental Validation of Subtethered Space Debris," *Journal of Guidance, Control, and Dynamics*, Vol. 41, No. 2, 2018, pp. 519–525. https://doi.org/10.2514/1.G003049.

[24] Hughes, P. C., *Spacecraft Attitude Dynamics*, Dover, Mineola, NY, 2004, pp. 93–99, 24–26, 232–238.

[25] Shabana, A. A., Hussien, H., and Escalona, J., "Application of the Absolute Nodal Coordinate Formulation to Large Rotation and Large Deformation Problems," *Journal of Mechanical Design*, Vol. 120, No. 2, 1998, pp. 188–195. https://doi.org/10.1115/1.2826958.

[26] Gerstmayr, J., and Shabana, A. A., "Analysis of Thin Beams and Cables Using the Absolute Nodal Co-Ordinate Formulation," *Nonlinear Dynamics*, Vol. 45, Nos. 1–2, 2006, pp. 109–130. https://doi.org/10.1007/s11071-006-1856-1

[27] Newmark, N. M., "A Method of Computation for Structural Dynamics," *Journal of Engineering Mechanics*, Vol. ASCE 85, No. EM3, 1959, pp. 67–94.

M. A. Ayoubi
Associate Editor